

for *Astrophysical Journal*, January 20, 2010

Atmospheric Chemistry in Giant Planets, Brown Dwarfs, and Low-Mass Dwarf Stars III. Iron, Magnesium, and Silicon

Channon Visscher^{1,2}, Katharina Lodders¹, and Bruce Fegley, Jr.¹

¹*Planetary Chemistry Laboratory, Department of Earth & Planetary Sciences, McDonnell Center for the Space Sciences, Washington University, St. Louis, MO 63130-4899*

²*Current Address: Lunar and Planetary Institute, USRA, Houston, TX 77058-1113*

visscher@lpi.usra.edu, lodders@wustl.edu, bfegley@wustl.edu

ABSTRACT

We use thermochemical equilibrium calculations to model iron, magnesium, and silicon chemistry in the atmospheres of giant planets, brown dwarfs, extrasolar giant planets (EGPs), and low-mass stars. The behavior of individual Fe-, Mg-, and Si-bearing gases and condensates is determined as a function of temperature, pressure, and metallicity. Our results are thus independent of any particular model atmosphere. The condensation of Fe metal strongly affects iron chemistry by efficiently removing Fe-bearing species from the gas phase. Monatomic Fe is the most abundant Fe-bearing gas throughout the atmospheres of EGPs and L dwarfs and in the deep atmospheres of giant planets and T dwarfs. Mg- and Si-bearing gases are effectively removed from the atmosphere by forsterite (Mg_2SiO_4) and enstatite (MgSiO_3) cloud formation. Monatomic Mg is the dominant magnesium gas throughout the atmospheres of EGPs and L dwarfs and in the deep atmospheres of giant planets and T dwarfs. Silicon monoxide (SiO) is the most abundant Si-bearing gas in the deep atmospheres of brown dwarfs and EGPs, whereas SiH_4 is dominant in the deep atmosphere of Jupiter and other gas giant planets. Several other Fe-, Mg-, and Si-bearing gases become increasingly important with decreasing effective temperature. In principle, a number of Fe, Mg, and Si gases are potential tracers of weather or diagnostic of temperature in substellar atmospheres.

Subject headings: astrochemistry — planets and satellites: individual (Jupiter) — stars: low-mass, brown dwarfs — stars: individual (Gliese 229B, HD 209458)

1. Introduction

Thermochemical models have been used to describe alkali (Lodders 1999), titanium and vanadium (Lodders 2002), carbon, nitrogen, and oxygen (Lodders & Fegley 2002), sulfur and phosphorus (Visscher et al. 2006), condensate (e.g., Lodders & Fegley 2006; Lodders 2009) chemistry in the atmospheres of gas giant planets, brown dwarfs, and low-mass dwarf stars. Here we continue and extend these previous studies by using thermochemical equilibrium calculations to model the chemical behavior of Fe, Mg, and Si in substellar objects. Iron, magnesium, and silicon are the most abundant rock-forming elements in a solar composition gas, and – condensed as iron metal (Fe), and forsterite (Mg_2SiO_4) and enstatite (MgSiO_3) – will produce the most massive cloud layers in substellar atmospheres. Cloud formation strongly affects the optical and infrared spectra of substellar objects by removing gases from the overlying atmosphere and by introducing solid or liquid cloud particles (e.g., Marley et al. 1996; Lodders 1999; Burrows et al. 2000; Lodders & Fegley 2006; Visscher et al. 2006; Lodders 2009).

The large and growing number of discovered brown dwarfs (>750) and extrasolar planets (>400) makes it impractical to model the thermochemistry of all objects individually (Lodders & Fegley 2002), as was done for Jupiter and Saturn (Fegley & Lodders 1994) and Gliese 229B (Fegley & Lodders 1996). Instead, we adopt an approach similar to that of our previous papers (Lodders & Fegley 2002; Visscher et al. 2006) and determine the abundance of each chemical species as a function of pressure, temperature, and metallicity, plotted in abundance contour diagrams. Our results are thus independent of any particular pressure-temperature profile, and in principle, the atmospheric profile for any object may be superimposed on the abundance diagrams to determine its equilibrium atmospheric chemistry. In some instances, the behavior of key gases may be diagnostic of atmospheric temperature and/or tracers of weather in substellar objects.

We begin with a brief description of our computational method (§2), and then present our results for iron chemistry in substellar atmospheres in §3. We first give an overview of iron chemistry in a solar composition gas and identify important gases and condensates (§3.1). This is followed by more detailed discussion of the chemical behavior individual Fe-bearing gases as a function of temperature, pressure, and metallicity (§3.2). Wherever possible, we note relevant spectroscopic observations of Fe-bearing gases in substellar objects. Our results for iron are then summarized by illustrating Fe gas chemistry along the atmospheric profiles of representative substellar objects (§3.3). A similar approach to magnesium and silicon chemistry follows in §4 and §5, respectively. We conclude with a brief summary in §6.

2. Computational Method

Thermochemical equilibrium calculations were performed using a Gibbs free energy minimization code, previously used for modeling the atmospheric chemistry of Saturn (Visscher et al. 2006) and sulfur and phosphorus chemistry in substellar objects (Visscher et al. 2006). Thermodynamic data for the equilibrium calculations were taken from the compilations of Gurvich et al. (1989-1994), Robie & Hemingway (1995), the fourth edition of the JANAF Tables (Chase 1998), and the thermodynamic database maintained in the Planetary Chemistry Laboratory (Lodders & Fegley 2002). This database includes additional thermodynamic data from the literature for compounds absent from the other compilations.

All calculations were conducted using elemental abundances from Lodders (2003) for a solar system (i.e., protosolar) composition gas. The effect of metallicity on sulfur and phosphorus chemistry was examined by running computations at $[\text{Fe}/\text{H}] = -0.5$ dex (subsolar), $[\text{Fe}/\text{H}] = 0$ dex (solar), and $[\text{Fe}/\text{H}] = +0.5$ dex (enhanced) metallicities. The metallicity factor, m , is defined as $\log m = [\text{Fe}/\text{H}]$. We assume that the elemental abundance ratios for Mg, Si, and other elements of interest vary similarly with $[\text{Fe}/\text{H}]$ (e.g., $[\text{Mg}/\text{H}] \approx [\text{Si}/\text{H}] \approx [\text{Fe}/\text{H}]$) over the range of metallicities considered here (see Edvardsson et al. 1993; Chen et al. 2000; Huang et al. 2005). When considering the chemical behavior of individual gases, we focus on higher temperatures (800 K and higher), where thermochemical processes are expected to dominate over disequilibrium processes such as photochemistry or atmospheric mixing (e.g., see Visscher et al. 2006).

We assume that condensates settle gravitationally into a cloud layer and are removed from the cooler, overlying atmosphere. This equilibrium cloud condensate scenario for the deep atmospheres of giant planets and brown dwarfs is supported by several lines of evidence (e.g., see Lodders & Fegley 2006, and references therein). First, the presence of germane (GeH_4) and the absence of silane (SiH_4) in the upper atmospheres of Jupiter and Saturn (even though Si is expected to be much more abundant than Ge) can be explained by the removal of Si from the gas into silicate clouds deeper in the atmosphere, whereas Ge remains in the gas phase (Fegley & Prinn 1988; Fegley & Lodders 1994). Secondly, the detection of H_2S in Jupiter’s troposphere by the *Galileo* entry probe indicates that Fe must be sequestered into a cloud layer at deep atmospheric levels, because the formation of FeS would otherwise remove H_2S from the gas above the ~ 700 K level (Lodders & Fegley 2002; Visscher et al. 2006). Third, absorption from monatomic K gas in the spectra of T dwarfs (Burrows et al. 2000; Geballe et al. 2001) requires the removal of Al and Si at deeper atmospheric levels, because K would otherwise be removed from the observable atmosphere by the condensation of orthoclase (KAlSi_3O_8) (Lodders & Fegley 2006). The presence of monatomic Na gas in brown dwarfs (Kirkpatrick et al. 1999; Burgasser et al. 2003; McLean et al. 2003;

Cushing et al. 2005) also suggests Al and Si removal, because albite ($\text{NaAlSi}_3\text{O}_8$) condensation would otherwise effectively remove Na from the observable atmosphere. Furthermore, the removal of Na by Na_2S cloud formation is consistent with the observed weakening of Na atomic lines throughout the L dwarf spectral sequence and their disappearance in early T dwarfs (e.g., Kirkpatrick et al. 1999; McLean et al. 2003; Visscher et al. 2006). Finally, as we note below, the disappearance of iron, magnesium, and silicon spectral features in later spectral types is consistent with removal of these elements into cloud layers. In our thermochemical model, the abundances of Fe-, Mg-, and Si-bearing gases above the clouds are computed assuming saturation (equilibrium) vapor pressure. If supersaturation occurs, a condensate will form and settle toward the cloud layer to restore equilibrium.

3. Iron Chemistry

3.1. Overview of Iron Chemistry

Figure 1 illustrates model atmospheric profiles for an M dwarf ($T_{\text{eff}} = 2600$ K, $\log g = 5.0$; Tsuji et al. 1996), an L dwarf ($T_{\text{eff}} = 1800$ K, $\log g = 5.0$; Burrows et al. 2006), the hot, close-in (Pegasi) planet HD209458b ($T_{\text{eff}} = 1350$ K; Iro et al. 2005), the T dwarf Gliese 229B ($T_{\text{eff}} = 960$ K; Marley et al. 1996), and Jupiter ($T_{\text{eff}} = 124$ K), indicated by dashed lines. We note that Jovian atmospheric chemistry differs slightly than that for a solar-metallicity gas because Jupiter has a heavy element enrichment comparable to $[\text{Fe}/\text{H}] \approx +0.5$ dex (Lodders 1999; Lodders & Fegley 2002).

Also shown in Figure 1 are lines indicating where $A(\text{CH}_4) = A(\text{CO})$ and $A(\text{H}_2) = A(\text{H})$. These boundaries are important because carbon and oxygen affect the chemical behavior of many Fe, Mg, and Si-bearing gases. Methane is the dominant carbon-bearing gas in Jupiter and T dwarfs (such as Gliese 229B) whereas CO is the dominant carbon-bearing gas in L dwarfs and Pegasi planets (such as HD209458b). Molecular hydrogen dissociates into monatomic H at high temperatures and low pressures (lower right corner of Figure 1). However, H_2 is the dominant form of hydrogen in substellar objects, and we therefore take $X_{\text{H}_2} \approx X_{\Sigma\text{H}} \approx 0.84$ throughout the following. This approximation holds for metallicities up to $[\text{Fe}/\text{H}] \approx +0.5$ dex; at higher metallicities the H_2 mole fraction abundance decreases as the relative abundance of heavy elements increases (e.g., $X_{\text{H}_2} \approx 0.82$ at $[\text{Fe}/\text{H}] \approx +1.0$ dex).

The dotted line in Figure 1 shows the condensation curve for Fe metal, with an open circle denoting its normal melting point (1809 K). Iron condensation occurs via



The equilibrium condensation temperature (T_{cond}) of Fe is approximated by

$$10^4/T_{\text{cond}}(\text{Fe}) = 5.44 - 0.48 \log P_T - 0.48[\text{Fe}/\text{H}], \quad (2)$$

where higher pressures and/or metallicities lead to higher Fe condensation temperatures. Iron cloud formation effectively removes nearly all iron from the atmosphere, and the abundances of Fe-bearing gases above the clouds rapidly decrease with altitude.

Monatomic Fe gas is the dominant Fe-bearing gas in a protosolar composition gas until it is replaced by $\text{Fe}(\text{OH})_2$ at low temperatures and high pressures. The conversion between Fe and $\text{Fe}(\text{OH})_2$ is represented by the net thermochemical reaction



and the solid line dividing the Fe and $\text{Fe}(\text{OH})_2$ fields in Figure 1 indicates where these gases have equal abundances $A(\text{Fe}) = A(\text{Fe}(\text{OH})_2) \approx \frac{1}{2}\Sigma\text{Fe}_{\text{gas}}$, where $\Sigma\text{Fe}_{\text{gas}}$ is the total amount of iron in the gas. The position of this line is given by

$$\log P_T = 11.94 - 12088/T - 2[\text{Fe}/\text{H}], \quad (4)$$

showing that an increase in metallicity will shift the Fe- $\text{Fe}(\text{OH})_2$ boundary to higher temperatures and lower pressures. In other words, an increase in metallicity increases the stability field of $\text{Fe}(\text{OH})_2$ for otherwise constant conditions.

3.2. Chemical Behavior of Iron-bearing Gases

3.2.1. Monatomic Iron, Fe

The mole fraction abundance of monatomic Fe as a function of pressure and temperature is shown in Figure 2a. As mentioned above, monatomic Fe is the dominant Fe-bearing gas over a wide range of pressures and temperatures in a solar system composition gas. Below the Fe clouds, the abundance of Fe gas is representative of the total iron content of the atmosphere ($X_{\text{Fe}} \approx X_{\Sigma\text{Fe}}$), and its abundance is given by

$$\log X_{\text{Fe}} \approx -4.24 + [\text{Fe}/\text{H}]. \quad (5)$$

Upon Fe metal condensation, the amount of iron in the gas rapidly decreases and the equilibrium Fe gas abundance is governed by its vapor pressure over solid or liquid iron, represented in reaction (1). The mole fraction abundance of monatomic Fe above the clouds is given by

$$\log X_{\text{Fe}} \approx 7.23 - 20995/T - \log P_T, \quad (6)$$

inversely proportional to P_T . The Fe gas abundance is independent of metallicity in this region because it depends solely on the temperature-dependent vapor pressure of iron. As described below (see §3.2.2 and §3.2.3), this expression can be used with chemical equilibria to determine the abundances of other iron gases in substellar atmospheres. Equations giving the abundance of Fe (and other Fe-bearing gases) as a function of temperature, pressure, and metallicity below and above the Fe clouds are listed in Table 1.

Neutral monatomic Fe possesses several hundred spectral lines in the J and H bands (Meléndez & Barbuy 1999), and Fe I features are observed in the spectra of brown dwarfs and low-mass dwarf stars (e.g. Cushing et al. 2005). The strong Fe feature at $1.189 \mu\text{m}$ weakens in mid- to late-type M dwarf spectra and generally disappears in mid-type L dwarfs (McLean et al. 2003; Cushing et al. 2005). This trend is consistent with the removal of iron from the gas into an Fe metal cloud deck located deeper below the photosphere in objects with low effective temperatures (e.g. Burgasser et al. 2002b).

3.2.2. Iron Hydride, FeH

The chemical behavior of FeH in a protosolar composition gas is illustrated in Figure 2b. The conversion between Fe and FeH occurs via the net thermochemical reaction



Here we show how chemical equilibria may be used to derive equations giving the abundance of Fe-bearing species as a function of temperature, pressure, and metallicity. Rearranging the equilibrium constant expression for reaction (7) yields

$$\log X_{\text{FeH}} = \log X_{\text{Fe}} + 0.5 \log X_{\text{H}_2} + 0.5 \log P_T + \log K_7. \quad (8)$$

Using the Fe abundance from equation (5), the temperature dependence of K_7 ($\log K_7 \approx -1.85 - 1905/T$ from 800 to 2500 K), and the hydrogen abundance ($X_{\text{H}_2} \approx 0.84$), the FeH abundance between the H_2 -H boundary and the Fe cloud deck is given by

$$\log X_{\text{FeH}} \approx -6.13 - 1905/T + 0.5 \log P_T + [\text{Fe}/\text{H}], \quad (9)$$

proportional to $P_T^{0.5}$ and m . At high temperatures (> 2000 K) and low pressures ($< 10^{-2}$ bar) as monatomic H becomes increasingly abundant the H_2 abundance begins to decrease near the H_2 -H boundary. The reduced H_2 abundance, in turn, reduces FeH formation via reaction (7) and changes the chemical behavior of FeH at high temperatures and low pressures (i.e., lower right corner of Figure 2a).

Above the iron clouds, the Fe abundance in equation (6) is used in equation (8) to give

$$\log X_{\text{FeH}} \approx 5.34 - 22900/T - 0.5 \log P_T, \quad (10)$$

where X_{FeH} is proportional to $P_T^{-0.5}$ and independent of metallicity. The differences in chemical behavior of FeH below (equation 9) and above (equation 10) the Fe cloud deck are illustrated in the shape of the FeH abundance contours in Figure 2b. The sharp bends in the contours correspond to the Fe condensation curve in Figure 1.

Absorption bands from FeH are common in the near-infrared spectra of brown dwarfs (e.g. Kirkpatrick et al. 1999; McLean et al. 2003; Cushing et al. 2003, 2005). The most prominent FeH feature is the band located at $0.9896 \mu\text{m}$, which weakens throughout the L dwarf spectral sequence and in early T dwarfs (McLean et al. 2003; Nakajima et al. 2004; Cushing et al. 2005), consistent with the removal of iron into a cloud located deeper and deeper in the atmosphere. This feature unexpectedly strengthens again in mid-type T dwarf spectra (Burgasser et al. 2002a,b; Nakajima et al. 2004; Cushing et al. 2005), prompting different explanations for the shape of the color-magnitude diagram for brown dwarfs near the L-T transition. Nakajima et al. (2004) suggested that the strengthening FeH bands are caused by upward convective mixing of FeH gas from deeper levels where it is more abundant. However, as pointed out by Burgasser et al. (2002b) and demonstrated Lodders & Fegley (2006), the fragile Fe—H bond is unlikely to survive convective upwelling in a T dwarf atmosphere. Instead, the observations are plausibly explained by cloud disruption and clearing (in a $\sim 1 \mu\text{m}$ window) which allows the observation of FeH gas at deep atmospheric levels (Burgasser et al. 2002b; Lodders & Fegley 2006).

3.2.3. Iron Monohydroxide, FeOH

Mole fraction contours of FeOH are illustrated in Figure 2c. The equilibrium between Fe and FeOH is represented by the net thermochemical reaction



and expressions giving the FeOH abundance as a function of temperature, pressure, and metallicity are listed in Table 1. Above the iron clouds, the curvature in the FeOH abundance contours along the CH_4 -CO boundary results from the effect of carbon chemistry on the H_2O abundance in reaction (11) (e.g. Lodders & Fegley 2002). For example, the atmospheric water abundance may be written as

$$\log X_{\text{H}_2\text{O}} = \log X'_{\text{H}_2\text{O}} + [\text{Fe}/\text{H}], \quad (12)$$

where $X'_{\text{H}_2\text{O}}$ is the water abundance in a solar-metallicity gas, which is $\log_{10} X'_{\text{H}_2\text{O}} \approx 10^{-3.12}$ inside the CH_4 field and $X'_{\text{H}_2\text{O}} \approx 10^{-3.58}$ inside the CO field in Figure 1. At temperatures and pressures near the CH_4 -CO boundary, $X'_{\text{H}_2\text{O}}$ may be derived from CH_4 -CO equilibria (Lodders & Fegley 2002). Rearranging the equilibrium constant expression for reaction (11) gives

$$\log X_{\text{FeOH}} = \log X_{\text{Fe}} + \log X_{\text{H}_2\text{O}} - 0.5 \log X_{\text{H}_2} + 0.5 \log P_T + \log K_{11}. \quad (13)$$

Substituting for the Fe abundance from equation (6), the H_2O abundance from equation (12), the H_2 abundance ($X_{\text{H}_2} \approx 0.8384$), and the temperature dependence of K_{11} ($\log K_{11} \approx -2.25 + 2468/T$ from 800 to 2500 K), equation (13) becomes

$$\log X_{\text{FeOH}} \approx 5.02 - 18527/T - 0.5 \log P_T + 2[\text{Fe}/\text{H}] + \log X'_{\text{H}_2\text{O}}. \quad (14)$$

This expression gives the FeOH abundance above the iron clouds and includes the effect of metallicity on the atmospheric water abundance. The kinks in the FeOH contours denote the position of the Fe condensation curve. As demonstrated in equation (14) and shown in Figure 2c, the mole fraction abundance of FeOH is proportional to $P_T^{-0.5}$ throughout this region.

3.2.4. Iron Hydroxide, $\text{Fe}(\text{OH})_2$

The chemical behavior of $\text{Fe}(\text{OH})_2$ as a function of temperature and pressure is illustrated in Figure 2d. The equilibrium conversion between Fe and $\text{Fe}(\text{OH})_2$ is represented by reaction (3). Below the Fe clouds (kinks in abundance contours), the $\text{Fe}(\text{OH})_2$ abundance increases with total pressure, and has a strong m^3 dependence on metallicity (see Table 1).

The $\text{Fe}(\text{OH})_2$ abundance in reaction (3) is very sensitive to the H_2O abundance since the formation of one mole of iron hydroxide requires two moles of water. As a result, there is a large shift in the $\text{Fe}(\text{OH})_2$ abundance contours above the clouds (inflections in Figure 2d) when moving between the CH_4 and CO fields. Within each field, the $\text{Fe}(\text{OH})_2$ abundance above the clouds is essentially pressure-independent (see Table 1) and is therefore, in principle, diagnostic of atmospheric temperature.

As shown in Figure 1, $\text{Fe}(\text{OH})_2$ becomes the most abundant Fe-bearing gas at low temperatures and high pressures in a solar composition gas. Iron hydroxide is therefore expected to be the most abundant iron gas at $T \lesssim 1600$ on Jupiter ($[\text{Fe}/\text{H}] \approx +0.5$) and $T \lesssim 1070$ on Gliese 229B. However, we emphasize that the amount of iron remaining in the gas is greatly diminished by the condensation of Fe metal at deeper atmospheric levels. For example, even where it is the most abundant Fe-bearing gas, the predicted $\text{Fe}(\text{OH})_2$ mole fraction is $\approx 10^{-12.6}$ at the 1000 K level in Jupiter’s atmosphere.

3.2.5. Iron Monoxide, FeO

Mole fraction abundance contours for FeO are shown in Figure 3a for a solar composition gas. Monatomic iron reacts with water to form FeO via the net reaction



Between the H_2 -H boundary and the Fe cloud deck, X_{FeO} is proportional to m^2 and is independent of pressure (see Table 1). In principle, the FeO abundance in this region is therefore diagnostic of either temperature or metallicity. Above the clouds, the FeO abundance decreases with pressure and increases with metallicity. As for FeOH and $\text{Fe}(\text{OH})_2$, the FeO abundance is sensitive to the H_2O abundance and the FeO abundance contours display a subtle shift along the CH_4 -CO equal abundance boundary.

3.2.6. Iron Sulfide, FeS

The abundance of FeS gas as a function of temperature and pressure is illustrated in Figure 3b. The chemical behavior of FeS is governed by the reaction between Fe and H_2S :



Above the iron clouds, H_2S is the dominant sulfur-bearing gas ($\log X_{\text{H}_2\text{S}} \approx -4.52 + [\text{Fe}/\text{H}]$), and the FeS abundance is proportional to P_T^{-1} and m (see Table 1). Below the Fe cloud deck, the FeS abundance is ~ 10 ppb and decreases at higher temperatures and lower pressures as H_2S is replaced by SH and S (Visscher et al. 2006). Iron sulfide is predicted to be the second or third most abundant iron gas throughout L dwarf atmospheres and in the upper atmospheres (< 1500 K) of Pegasi planets.

3.3. Iron Chemistry in Substellar Objects

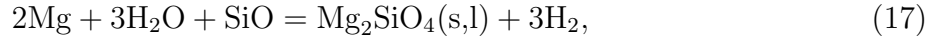
Figures 4a-4d summarize the iron gas chemistry in four representative substellar objects: Jupiter, the T dwarf Gliese 229B, the Pegasi planet HD209458b, and an L dwarf ($T_{\text{eff}} = 1800$ K). Iron chemistry in substellar objects is strongly affected by Fe metal condensation at deep atmospheric levels. Monatomic Fe is the dominant Fe-bearing gas in the deep atmospheres of Jupiter and Gliese 229B, and throughout the atmospheres of HD209458b and the L dwarf. A number of Fe-bearing gases become relatively more abundant in objects with lower effective temperatures. On Jupiter and Gliese 229B, $\text{Fe}(\text{OH})_2$ replaces Fe at lower temperatures. The $\text{Fe}(\text{OH})_2$ and FeO abundances are pressure-independent and thus potentially diagnostic of

atmospheric temperature, respectively, above and below the iron clouds. For all four objects, iron hydride (FeH) is the second most abundant Fe-bearing gas at deep atmospheric levels, until it is replaced at lower temperatures by Fe(OH)₂, FeOH, or FeS. Because of its strong absorption and relatively high abundance near the iron condensation level, FeH is a tracer of weather in brown dwarfs (e.g. Burgasser et al. 2002b). Other Fe-bearing gases (e.g. Fe, FeOH, FeS) are potential tracers of weather since they typically achieve their maximum abundance near iron cloud base.

4. Magnesium Chemistry

4.1. Overview of Magnesium Chemistry

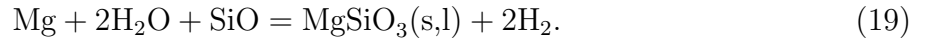
Figure 5 gives an overview of Mg chemistry as a function of pressure and temperature in a protosolar composition gas. The dotted lines labeled Mg₂SiO₄(s,l), MgSiO₃(s,l), and MgO(s) show the equilibrium condensation curves for forsterite, enstatite, and periclase, respectively, and the open circles denote the normal melting temperatures for forsterite (2163 K) and enstatite (1830 K). Forsterite (Mg₂SiO₄) condenses via the net thermochemical reaction



and its condensation temperature as a function of pressure and metallicity is approximated by

$$10^4/T_{\text{cond}}(\text{Mg}_2\text{SiO}_4) \approx 5.89 - 0.37 \log P_T - 0.73[\text{Fe}/\text{H}], \quad (18)$$

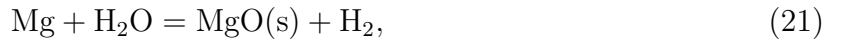
At slightly lower temperatures, enstatite (MgSiO₃) condensation occurs via the net reaction



The enstatite condensation curve is approximated by

$$10^4/T_{\text{cond}}(\text{MgSiO}_3) \approx 6.26 - 0.35 \log P_T - 0.70[\text{Fe}/\text{H}], \quad (20)$$

where higher pressures and/or metallicities lead to higher condensation temperatures. At very high pressures, forsterite and enstatite condensation temperature are depressed as SiO is replaced by SiH₄ (see §5.1). Periclase (MgO) condenses via the net thermochemical reaction

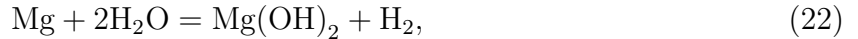


at pressures greater than 10^{3.5} bar. The condensation curve for akermanite (Ca₂MgSi₂O₇) is not shown here because most Ca is expected to be removed at deeper atmospheric levels

by the condensation of refractory calcium aluminates (e.g., Lodders 2002). If no calcium is removed, $\text{Ca}_2\text{MgSi}_2\text{O}_7$ condensation would consume $\sim 3\%$ of the total atmospheric Mg inventory. In the same way, olivine $((\text{Mg,Fe})_2\text{SiO}_4)$ and fayalite $(\text{Fe}_2\text{SiO}_4)$ are not expected in substellar atmospheres because nearly all Fe is removed from the gas phase by iron metal condensation at higher temperatures (e.g., Cushing et al. 2006; Lodders & Fegley 2006)

Magnesium-silicate cloud formation is very effective at removing nearly all ($>99\%$) magnesium from the atmosphere, and the abundances of Mg-bearing gases rapidly decrease with altitude above the clouds. This behavior is generally consistent with the disappearance of Mg spectral features by early-type L dwarfs (see §4.2.1). Furthermore, Cushing et al. (2006) find a Si—O absorption feature at $10\ \mu\text{m}$ in mid-type L dwarfs which is consistent with the presence of silicate grains and a weak $9.17\ \mu\text{m}$ feature tentatively attributed to crystalline enstatite.

Monatomic Mg is the dominant Mg-bearing gas in substellar atmospheres until it is replaced by $\text{Mg}(\text{OH})_2$ at low temperatures and high pressures. The conversion between Mg and $\text{Mg}(\text{OH})_2$ is represented by the net thermochemical reaction



and the solid line in Figure 5 indicates where Mg and $\text{Mg}(\text{OH})_2$ have equal abundances $A(\text{Mg}) = A(\text{Mg}(\text{OH})_2) \approx \frac{1}{2}\Sigma\text{Mg}_{\text{gas}}$, where $\Sigma\text{Mg}_{\text{gas}}$ is the total amount of magnesium in the gas. The position of the equal-abundance line is given by

$$\log P_T = 10.96 - 10267/T - 2[\text{Fe}/\text{H}], \quad (23)$$

where an increase in metallicity shifts the Mg- $\text{Mg}(\text{OH})_2$ boundary to higher temperatures and lower pressures.

4.2. Chemical Behavior of Magnesium-bearing Gases

4.2.1. Monatomic Magnesium, Mg

Figure 6a shows the chemical behavior of monatomic Mg as a function of pressure and temperature in a solar-metallicity gas. The chemical behavior of Mg is strongly affected by silicate cloud formation. Below the forsterite clouds, the abundance of Mg gas is given by

$$\log X_{\text{Mg}} \approx -4.15 + [\text{Fe}/\text{H}], \quad (24)$$

and comprises nearly 100% of the total elemental Mg content in the atmosphere ($X_{\text{Mg}} \approx X_{\Sigma\text{Mg}}$). Upon forsterite and enstatite condensation, the magnesium gas abundance is governed by its vapor pressure over rock, represented by reactions (17) and (19). Curvature

in the Mg mole fraction contours in Figure 6a occurs along the CH₄-CO boundary, which affects the H₂O abundance in reactions (17) and (19). The Mg abundance is therefore

$$\log X_{\text{Mg}} \approx 11.37 - 27250/T - \log P_T - [\text{Fe}/\text{H}]. \quad (25)$$

in CH₄-dominated objects, and

$$\log X_{\text{Mg}} \approx 11.83 - 27250/T - \log P_T - [\text{Fe}/\text{H}]. \quad (26)$$

in CO-dominated objects. We can use these expressions along with chemical equilibria to determine the abundances of other Mg-bearing gases in substellar atmospheres. Equations giving the abundance of Mg-bearing gases as a function of pressure, temperature, and metallicity in a protosolar composition gas are listed in Table 2.

Several Mg absorption lines are present in the near infrared spectra of M dwarfs, including the prominent feature at 1.183 μm (Jones et al. 1996; McLean et al. 2003; Cushing et al. 2005). These features weaken in mid- to late-type M dwarfs and generally disappear by \sim L1 (Cushing et al. 2005), consistent with the removal of magnesium into Mg₂SiO₄ and MgSiO₃ clouds located at increasingly greater depths below the observable atmosphere (e.g., see Lodders 2004; Lodders & Fegley 2006).

4.2.2. Magnesium Hydride, MgH

Mole fraction contours for MgH are illustrated in Figure 6b. The MgH abundance is governed by equilibrium with monatomic Mg, via the net thermochemical reaction



Between the H₂-H boundary and the Mg-silicate cloud base, the MgH abundance is proportional to $P_T^{0.5}$ and m^1 (see Table 2). In contrast, the MgH abundance above the magnesium-silicate clouds is proportional to $P_T^{-0.5}$ and m^{-1} . The sharp bends in the MgH abundance contours occur at the condensation temperature of forsterite. Slight inflections in the MgH abundance occur along the CH₄-CO boundary, because the Mg abundance in reaction (27) is sensitive to the H₂O abundance in reactions (17) and (19). Magnesium hydride is an important opacity source from 0.44 to 0.56 μm (Weck et al. 2003), and MgH bands at 0.48 and 0.52 μm have been found in the optical spectra of bright L dwarfs and extreme subdwarfs (Kirkpatrick et al. 1999; Reid et al. 2000; Kirkpatrick 2005).

4.2.3. Magnesium Monohydroxide, $MgOH$

The chemical behavior of $MgOH$ as a function of pressure and temperature is shown in Figure 6c. The equilibrium abundance of $MgOH$ is governed by the reaction



decreasing with temperature and proportional to $P_T^{0.5}$ and m^2 below the Mg-silicate clouds. The kinks in the $MgOH$ contours occur where forsterite condenses. Above the clouds, X_{MgOH} is proportional to $P_T^{-0.5}$ (see Table 2). Interestingly, the $MgOH$ abundance in this region is independent of metallicity and shows no shift at the CH_4 -CO boundary because these effects cancel out in reaction (28). For example, the H_2O abundance slightly decreases when moving from the CH_4 to the CO field (e.g. Lodders & Fegley 2002). However, as can be seen by comparing equations (25) and (26), there is a corresponding increase in the Mg abundance, so the resulting $MgOH$ abundance in reaction (28) remains unaffected by carbon chemistry. Magnesium monohydroxide is typically the third most abundant Mg-bearing gas in substellar atmospheres.

4.2.4. Magnesium Hydroxide, $Mg(OH)_2$

Mole fraction abundance contours for $Mg(OH)_2$ are shown in Figure 6d for a solar-metallicity gas. The equilibrium conversion between Mg and $Mg(OH)_2$ is represented by reaction (22). Below the Mg-silicate clouds, the $Mg(OH)_2$ abundance decreases with temperature and pressure, and has a very strong (m^3) dependence on metallicity.

Above the magnesium-silicate clouds (the kinks in Figure 6d), the $Mg(OH)_2$ abundance contours show inflections along the CH_4 -CO boundary, because $Mg(OH)_2$ is sensitive to the water abundance in reaction (22). Within either the CH_4 or CO field, the $Mg(OH)_2$ abundance is pressure-independent. In principle, the abundance of $Mg(OH)_2$ is therefore diagnostic of atmospheric temperature if the object’s metallicity is known.

At low temperatures and high pressures, $Mg(OH)_2$ becomes the most abundant Mg-bearing gas, as illustrated in Figure 5. Magnesium hydroxide is thus expected to be the dominant magnesium gas below ~ 1550 K in the atmosphere of Jupiter (cf. Fegley & Lodders 1994) and below ~ 980 K on Gliese 229B.

4.2.5. *Magnesium Monoxide, MgO*

The abundance of MgO as a function of pressure and temperature is illustrated in Figure 7a. Magnesium monoxide forms via the net thermochemical reaction



Below the Mg-silicate cloud deck, at pressures less than ~ 10 bar, the MgO abundance is effectively pressure-independent and is therefore potentially diagnostic of atmospheric temperature if the metallicity is known.

For similar reasons as for MgOH (see §4.2.3), the MgO abundance above the magnesium-silicate clouds is independent of metallicity and is unaffected by the CH₄-CO boundary. For example, the Mg abundance decreases with metallicity, as shown by equations (25) and (26), whereas the H₂O abundance increases with metallicity. These effects cancel out in reaction (29), with the result that MgO is unaffected by changes in metallicity or the prevailing carbon chemistry.

4.2.6. *Magnesium Sulfide, MgS*

Figure 7b displays mole fraction contours for MgS in protosolar composition gas. The equilibrium abundance of MgS is governed by the reaction



Near the silicate cloud base, the MgS abundance is ~ 10 ppb in a solar-metallicity gas and decreases at higher temperatures and lower pressures as H₂S is replaced by monatomic S. Above the Mg-silicate clouds, X_{MgS} is proportional to P_T^{-1} and is metallicity-independent (see Table 2). Magnesium sulfide is typically among the more abundant Mg-bearing gases in brown dwarfs and extrasolar giant planets, and becomes the second most abundant magnesium gas at temperatures below ~ 1600 K in the atmospheres of L dwarfs and Pegasi planets.

4.3. **Magnesium Chemistry in Substellar Objects**

Magnesium gas chemistry along the pressure-temperature profiles of Jupiter, Gliese 229B, HD209458b, and an L dwarf ($T_{\text{eff}} = 1800$ K) are illustrated in Figures 8a-8d. Monatomic Mg is the dominant Mg-bearing gas throughout the atmospheres of Pegasi planets and L

dwarfs, and in the deep atmospheres of giant planets and T dwarfs. Furthermore, the Mg abundance below the Mg-silicate cloud deck is essentially constant and representative of the total Mg abundance in the atmosphere. Upon condensation, the abundances of magnesium-bearing gases rapidly decrease with decreasing temperature above the magnesium-silicate clouds. In objects with lower effective temperatures, a number of other Mg-bearing gases become relatively abundant and $\text{Mg}(\text{OH})_2$ replaces Mg as the most abundant magnesium gas at the ~ 1550 K level on Jupiter and the ~ 980 K level on Gliese 229B. Magnesium hydride (MgH) is the second most abundant magnesium gas in the deep atmospheres of substellar objects until it is replaced at lower temperatures by $\text{Mg}(\text{OH})_2$ and MgOH (in giant planets and T dwarfs) or MgS (in L dwarfs and Pegasi planets). Magnesium hydroxide ($\text{Mg}(\text{OH})_2$) and MgO are potential atmospheric temperature probes, respectively, above and below the magnesium-silicate clouds.

5. Silicon Chemistry

5.1. Overview of Silicon Chemistry

An overview of silicon chemistry as a function of pressure and temperature is illustrated in Figure 9. The dotted lines labeled $\text{Mg}_2\text{SiO}_4(\text{s,l})$ and $\text{MgSiO}_3(\text{s,l})$ show the condensation temperatures of forsterite and enstatite, which together remove nearly all silicon from the overlying atmosphere. Cushing et al. (2006) found that silicate absorption features near $10\ \mu\text{m}$ in mid-type L dwarf spectra are consistent with the presence of these magnesium silicates, but noted the possibility of additional absorption by quartz (SiO_2) grains based upon the predictions of Helling et al. (2006). In contrast to the models of Helling et al. (2006, 2008), we find that quartz will not condense in the atmospheres of substellar objects unless enstatite condensation is suppressed. This is demonstrated in Figure 10, which shows the elemental distribution of Si in condensed phases at 1 bar total pressure in a solar-metallicity gas with (Figure 10a) and without (Figure 10b) enstatite condensation. As shown in Figure 10, Mg_2SiO_4 formation consumes nearly half of the total Si abundance because the solar elemental abundances of Mg and Si are approximately equal. Enstatite formation plausibly proceeds via reactions between SiO gas and pre-existing forsterite grains and continues until nearly all silicon is consumed. Thus, quartz ($T_{\text{cond}} \sim 1550$ K) can only form in the absence of enstatite ($T_{\text{cond}} \sim 1600$ K), because MgSiO_3 otherwise efficiently removes silicon from the gas phase. Even in the absence of gas-grain reactions between SiO and Mg_2SiO_4 , the vapor pressures of Mg and SiO above forsterite (reaction 17) remain high enough to drive enstatite cloud formation via the net thermochemical reaction (19), so that MgSiO_3 condenses instead of SiO_2 . We therefore conclude that SiO_2 will not condense within the silicate cloud.

The most abundant Si-bearing gas over a wide range of pressures and temperatures is SiO, until it is replaced at higher pressures by silane, SiH₄ (see Figure 9). The equilibrium conversion between SiO and SiH₄ is



The position of the line where SiO and SiH₄ have equal abundances $A(\text{SiO}) = A(\text{SiH}_4) \approx \frac{1}{2}\Sigma\text{Si}_{\text{gas}}$ (where $\Sigma\text{Si}_{\text{gas}}$ is the total amount of silicon in the gas) is given by

$$\log P_T = 4.68 - 3086/T + 0.5[\text{Fe}/\text{H}]. \quad (32)$$

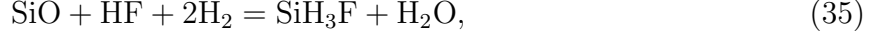
As temperatures decrease, SiH₄ is replaced by SiH₃F via the net thermochemical reaction



This reaction is independent of pressure and the position of the SiH₄-SiH₃F boundary is given by

$$T = 6948/(7.24 - [\text{Fe}/\text{H}]), \quad (34)$$

and occurs at $T \sim 960$ K in a solar-metallicity gas. Meanwhile, The equilibrium between SiO and SiH₃F is



where the position of the SiO-SiH₃F line is given by

$$\log P_T = 8.30 - 6560/T, \quad (36)$$

independent of the metallicity. The SiH₄-SiO, SiH₄-SiH₃F, and SiO-SiH₃F equal abundance lines intersect to form a “triple point” at $T \sim 960$ K and $P_T \sim 10^{1.47}$ bar in solar-metallicity gas, where all three gases have equal abundances $[A(\text{SiO}) = A(\text{SiH}_4) = A(\text{SiH}_3\text{F}) \approx \frac{1}{3}\Sigma\text{Si}_{\text{gas}}]$.

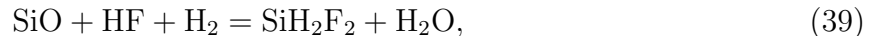
At lower temperatures, SiH₂F₂ replaces SiH₃F via the net thermochemical reaction



This reaction is also independent of pressure and the SiH₃F-SiH₂F₂ boundary is given by

$$T = 7040/(7.68 - [\text{Fe}/\text{H}]), \quad (38)$$

and is located at $T \sim 917$ K in a solar-metallicity gas. The conversion between SiO and SiH₂F₂ takes place by the reaction



where the position of the SiO-SiH₂F₂ boundary is given by

$$\log P_T = 12.14 - 10080/T - 0.5[\text{Fe}/\text{H}]. \quad (40)$$

In a solar-metallicity gas, equations (36) and (40) intersect to form the SiO-SiH₃F-SiH₂F₂ “triple point” at $T \sim 917$ K and $P_T \sim 10^{1.15}$ bar, where all three gases have equal abundances ($X \approx 10^{-19.4}$ for $[\text{Fe}/\text{H}] = 0$). However, the abundances of SiH₃F and SiH₂F₂ in this region are extremely low because most silicon is removed from the atmosphere by cloud formation at deeper levels.

5.2. Chemical Behavior of Silicon-bearing Gases

5.2.1. Silicon Monoxide, SiO

The chemical behavior of SiO in a protosolar composition gas is illustrated in Figure 11 as a function of pressure and temperature. Within the SiO field, the SiO abundance below the magnesium-silicate clouds is given by

$$\log X_{\text{SiO}} \approx -4.20 + [\text{Fe}/\text{H}], \quad (41)$$

and SiO contains $\sim 100\%$ of the atmospheric silicon inventory ($X_{\text{SiO}} \approx X_{\Sigma\text{Si}}$). Upon Mg-silicate condensation, silicon is efficiently removed from the gas phase and the SiO abundance rapidly decreases with decreasing temperature. Above the clouds, the SiO abundance is governed by its vapor pressure over rock. Curvature in the SiO contour lines along the CH₄-CO equal abundance boundary results from the effect of carbon chemistry on the H₂O abundance in reactions (17) and (19). The SiO abundance is thus

$$X_{\text{SiO}} \approx 13.21 - 28817/T - \log P_T - [\text{Fe}/\text{H}], \quad (42)$$

in CH₄-dominated objects and

$$X_{\text{SiO}} \approx 13.67 - 28817/T - \log P_T - [\text{Fe}/\text{H}], \quad (43)$$

in CO-dominated objects, inversely proportional to pressure and metallicity. These expressions, along with chemical equilibria, are used to determine the equilibrium abundances of other Si-bearing gases. Expressions giving the abundances of silicon species as a function of temperature, pressure, and metallicity in a protosolar composition gas are listed in Table 3. We note that the types of cloud condensates present will affect the gas chemistry of SiO and subsequently all other Si-bearing gases. For example, as shown in Figure 12, SiO

mole fraction abundances above the clouds are ~ 0.5 dex higher if enstatite formation is suppressed and replaced by SiO_2 condensation (see §5.1 above). The SiO abundance is therefore potentially diagnostic of weather and cloud composition in brown dwarf atmospheres.

Silicon monoxide has not yet been detected in the atmospheres of brown dwarfs or giant planets, but has been observed in numerous objects including molecular clouds, circumstellar envelopes, the photospheres of late-type stars, and sunspots (e.g., Campbell et al. 1995, and references therein). Abundant SiO gas was recently detected in the circumstellar disk of the β Pic analog HD172555 (Lisse et al. 2009).

5.2.2. Silicon Monosulfide, SiS

Mole fraction contours for SiS are shown in Figure 13a for a solar-metallicity gas. Silicon monosulfide is formed by the reaction between SiO and H_2S :



Below the Mg-silicate cloud deck, $X_{\text{SiS}} \sim 5\text{-}10$ ppm in a solar-metallicity gas. The SiS abundance decreases at higher temperatures and lower pressures as H_2S is replaced by SH and monatomic S (e.g. Visscher et al. 2006).

Above the clouds, the SiS abundance is inversely proportional to metallicity and total pressure (see Table 3). The SiS abundance contours in Figure 13a also display curvature along the CH_4 -CO boundary. This shift is more pronounced for SiS than for SiO because the SiS abundance in reaction (44) depends on the SiO and H_2O abundances, both of which are affected by carbon chemistry. For example, when reaction (44) is at equilibrium, LeChâtelier’s principle shows that more SiS is produced either by adding SiO (or H_2S) or removing H_2O . When moving from the CH_4 field to the CO field in a protosolar composition gas, the SiO abundance increases and the H_2O abundance decreases, yielding a correspondingly large increase in the SiS abundance. Silicon sulfide is expected to be the second most abundant silicon-bearing gas (after SiO) in the atmospheres of brown dwarfs and extrasolar giant planets. Furthermore, it is a potential tracer of weather in these objects because its maximum abundance is typically achieved near the magnesium-silicate cloud base.

5.2.3. Monatomic Silicon, Si

Figure 13b illustrates the chemical behavior of monatomic Si gas as a function of pressure and temperature. The abundance of Si is governed by the net thermochemical reaction



Below the Mg-silicate cloud deck and at pressures less than ~ 10 bar, the Si abundance is effectively independent of pressure and metallicity and thus potentially diagnostic of atmospheric temperature. Above the clouds, the Si abundance rapidly decreases with decreasing temperature and is proportional to P_T^{-1} and m^{-2} (see Table 3). A number of Si absorption bands are observed in the near infrared spectra of low-mass dwarf stars. These features generally weaken and disappear in late-type M dwarfs (Cushing et al. 2005), consistent with the removal of silicon into Mg_2SiO_4 and MgSiO_3 clouds deeper in the atmosphere.

5.2.4. Silyldyne, SiH

The abundance of SiH as a function of pressure and temperature is illustrated in Figure 14a. The SiH abundance is governed by the net thermochemical reaction



Below the Mg-silicate clouds, the SiH abundance is proportional to $P_T^{0.5}$ and is independent of metallicity. Above the clouds, the SiH abundance is proportional to $P_T^{-0.5}$ and m^{-2} (see Table 3). When moving from the CH_4 to the CO field, the SiO abundance increases and the H_2O abundance decreases in reaction (46). Both effects serve to increase the SiH abundance, resulting in a shift in the SiH contour lines along the CH_4 -CO boundary. The m^{-2} dependence on metallicity means that for every $[\text{Fe}/\text{H}] = +1$ dex increase in metallicity, the SiH abundance decreases by a factor of 100 at a given pressure and temperature.

5.2.5. Silylene, SiH_2

Mole fraction contours for SiH_2 are shown in Figure 14b. The equilibrium between SiO and SiH_2 is given by the reaction



Beneath the magnesium-silicate cloud deck, the metallicity-independent silylene abundance increases with total pressure. Upon rock condensation, the amount of SiH_2 remaining in

the gas rapidly decreases with decreasing temperature. As for SiH, the SiH₂ abundance is sensitive to the SiO and H₂O abundances in reaction and thus a shift occurs in the SiH₂ contour lines when moving between the CH₄ and CO fields. Within each field, the SiH₂ abundance is pressure-independent (see Figure 14 and Table 3), and thus potentially diagnostic of temperature if the metallicity is known and SiH₂ is thermochemical in origin.

5.2.6. Silyl Radical, SiH₃

The chemical behavior of the SiH₃ radical in a solar-metallicity gas is illustrated in Figure 14c. The abundance of SiH₃ is governed by the reaction



Between the H₂-H boundary and the Mg-silicate cloud base, the SiH₃ is proportional to $P_T^{1.5}$. Above the clouds, the SiH₃ abundance is proportional to $P_T^{1.5}$ and m^{-2} (see Table 3). There is curvature in the SiH₃ contour lines along the CH₄-CO boundary because the prevailing carbon chemistry affects both the SiO and H₂O abundances in reaction (48)

5.2.7. Silane, SiH₄

Mole fraction abundance contours for SiH₄ are illustrated in Figure 14d. The equilibrium conversion between SiO and SiH₄ is represented by reaction (31), and expressions giving the SiH₄ abundance as a function of pressure, temperature, and metallicity are listed in Table 3. Below the clouds, the silane abundance has a strong (P_T^2) dependence on total pressure. Upon Mg-silicate cloud formation, there is an inflection in the SiH₄ contour lines, and the SiH₄ abundance above the clouds is proportional to P_T and m^{-2} . Curvature in the SiH₄ contour lines along the CH₄-CO boundary results from the effect of carbon chemistry on the SiO and H₂O abundances in reaction (31).

At high pressures and temperatures (> 960 K for $[\text{Fe}/\text{H}] = 0$), SiH₄ becomes the most abundant silicon-bearing gas. We thus expect SiH₄ to be the dominant silicon gas below the 1031 K level in the deep atmosphere of Jupiter ($[\text{Fe}/\text{H}] \approx +0.5$). However, we again emphasize the efficiency with which rock condensation removes silicon from the gas, and we expect an abundance of $X_{\text{SiH}_4} \approx 10^{-16.5}$ at the 1031 K level on Jupiter. At lower temperatures, SiH₄ is surpassed by SiH₃F and SiH₂F₂. Silane is expected to be the third most abundant Si-bearing gas in the deep atmosphere of Gliese 229B.

We also point out the trend in pressure dependence for the silicon hydrides below

($X_{\text{SiH}} \propto P_T^{0.5}$, $X_{\text{SiH}_2} \propto P_T^1$, $X_{\text{SiH}_3} \propto P_T^{1.5}$, $X_{\text{SiH}_4} \propto P_T^2$) and above the silicate clouds ($X_{\text{SiH}} \propto P_T^{-0.5}$, $X_{\text{SiH}_2} \propto P_T^0$, $X_{\text{SiH}_3} \propto P_T^{0.5}$, $X_{\text{SiH}_4} \propto P_T^1$), which is evident in the shapes of the contour lines in Figure 14. The abundance of each of the silicon hydrides is metallicity-independent below the Mg-silicate clouds and proportional to m^{-2} above the clouds.

5.3. Silicon Chemistry in Substellar Atmospheres

Figures 15a-15d summarize the chemical behavior of silicon gases along the pressure temperature profiles of Jupiter, the T dwarf Gliese 229B, the Pegasi planet HD209458b, and an L dwarf ($T_{\text{eff}} = 1800$ K). There is a clear trend in silicon chemistry as a function of effective temperature. On Jupiter, SiH_4 is the dominant Si-bearing gas throughout the deep atmosphere, and is replaced by SiH_3F and SiH_2F_2 at lower temperatures (see Figure 9). The second most abundant Si-bearing gas is SiO , followed by SiS and a number of other silicon gases. In the warmer atmosphere of Gliese 229B, SiO is the dominant Si-bearing gas, followed by SiS and SiH_4 . The relative importance of SiH_4 decreases with increasing effective temperature, and SiO and SiS are the most important silicon gases throughout the atmospheres of Pegasi planets and L dwarfs. The abundances of all the silicon gases shown in Figure 15 rapidly decrease with decreasing temperature above the silicate clouds, which explains the non-detection of SiH_4 and other silicon species in the atmospheres of Jupiter and Saturn. Below the cloud base, the important silicon gases SiO and SiS reach their maximum abundance and are therefore potential tracers of weather in brown dwarfs and Pegasi planets. Silylene (SiH_2) and monatomic silicon (Si) are potentially diagnostic of atmospheric temperature, respectively, above and below the magnesium silicate clouds. The abundant silicon gases SiO and SiS typically achieve their maximum abundance near the cloud base and are potential tracers of weather in brown dwarfs and Pegasi planets.

6. Summary

The chemical behavior of iron species in substellar atmospheres is strongly affected by Fe metal condensation, which efficiently removes most iron from the gas phase. Similarly, most magnesium and silicon is removed from the gas by forsterite (Mg_2SiO_4) and enstatite (MgSiO_3) cloud formation. The equilibrium abundances of Fe-, Mg-, and Si-bearing gases rapidly decrease with increasing altitude (and decreasing temperature) above the clouds.

Monatomic iron is the dominant Fe-bearing gas throughout the atmospheres of L dwarfs and Pegasi planets. Other less abundant iron gases become increasingly important in objects

with lower effective temperatures, and $\text{Fe}(\text{OH})_2$ replaces Fe at low temperatures in T dwarfs and giant planets. Magnesium gas chemistry is similar to that of iron. Monatomic Mg is the most abundant magnesium gas throughout the atmospheres of L dwarfs and Pegasi planets and in the deep atmospheres of giant planets and T dwarfs, where Mg is replaced by $\text{Mg}(\text{OH})_2$ at lower temperatures. A number of Mg-bearing gases become relatively abundant with decreasing effective temperature. Silicon monoxide (SiO) is the most abundant Si-bearing gas, followed by SiS, throughout the atmospheres of L dwarfs and Pegasi planets and in the deep atmospheres of T dwarfs. In objects with lower effective temperatures, a number of other silicon gases become increasingly important and SiH_4 is the dominant silicon gas in the deep atmosphere of Jupiter. At high pressures and low temperatures SiH_4 and SiO are replaced by SiH_3F and/or SiH_2F_2 .

The abundances of several Fe-, Mg-, and Si-bearing gases are pressure-independent and thus, in principle, diagnostic of atmospheric temperature. These include $\text{Fe}(\text{OH})_2$, $\text{Mg}(\text{OH})_2$, and Si below the clouds and FeO, MgO, and SiH_2 above the clouds. In addition, a number of gases (e.g. Fe, FeH, FeOH, FeS, Mg, MgH, MgOH, MgS, SiO, SiS) may serve as indicators of weather since they generally reach their maximum abundance just below the iron metal or magnesium-silicate cloud decks. This may be particularly useful for late M dwarfs and early L dwarfs in which the metal and silicate clouds are located at relatively shallow depths below the photosphere.

This research was conducted at Washington University in St. Louis and was supported by the NASA Planetary Atmospheres Program (NNG06GC26G). Support for K. Lodders was also provided by NSF Grant AST-0707377. Final preparation of the manuscript was supported by the Lunar and Planetary Institute/USRA (NASA Cooperative Agreement NCC5-679). LPI Contribution No. XXXX.

REFERENCES

- Burgasser, A. J. et al. 2002a, *Astrophysical Journal*, 564, 421
- Burgasser, A. J., Kirkpatrick, J. D., Liebert, J., & Burrows, A. 2003, *Astrophysical Journal*, 594, 510
- Burgasser, A. J., Marley, M. S., Ackerman, A. S., Saumon, D., Lodders, K., Dahn, C. C., Harris, H. C., & Kirkpatrick, J. D. 2002b, *Astrophysical Journal Letters*, 571, L151
- Burrows, A., Marley, M. S., & Sharp, C. M. 2000, *Astrophysical Journal*, 531, 438

- Burrows, A., Sudarsky, D., & Hubeny, I. 2006, *Astrophysical Journal*, 640, 1063
- Campbell, J. M., Klapstein, D., Dulick, M., Bernath, P. F., & Wallace, L. 1995, *Astrophysical Journal Supplement*, 101, 237
- Chase, M. W. 1998, *J. Phys. Chem. Ref. Data*, 28, monograph no. 9
- Chen, Y. Q., Nissen, P. E., Zhao, G., Zhang, H. W., & Benoni, T. 2000, *Astronomy and Astrophysics Supplement*, 141, 491
- Cushing, M. C., Rayner, J. T., Davis, S. P., & Vacca, W. D. 2003, *Astrophysical Journal*, 582, 1066
- Cushing, M. C., Rayner, J. T., & Vacca, W. D. 2005, *Astrophysical Journal*, 623, 1115
- Cushing, M. C. et al. 2006, *ApJ*, 648, 614
- Edvardsson, B., Andersen, J., Gustafsson, B., Lambert, D. L., Nissen, P. E., & Tomkin, J. 1993, *Astronomy and Astrophysics*, 275, 101
- Fegley, Jr., B., & Lodders, K. 1994, *Icarus*, 110, 117
- . 1996, *Astrophysical Journal Letters*, 472, L37
- Fegley, Jr., B., & Prinn, R. G. 1988, *Astrophysical Journal*, 324, 621
- Geballe, T. R., Saumon, D., Leggett, S. K., Knapp, G. R., Marley, M. S., & Lodders, K. 2001, *Astrophysical Journal*, 556, 373
- Gurvich, L. V., Veyts, I. V., & Alcock, C. B. 1989-1994, *Thermodynamic Properties of Individual Substances*, 3 vols., 4th edn. (New York: Hemisphere Publishing)
- Helling, C. et al. 2008, *MNRAS*, 391, 1854
- Helling, C., Thi, W., Woitke, P., & Fridlund, M. 2006, *A&A*, 451, L9
- Huang, C., Zhao, G., Zhang, H. W., & Chen, Y. Q. 2005, *Monthly Notices of the Royal Astronomical Society*, 363, 71
- Iro, N., Bézard, B., & Guillot, T. 2005, *Astronomy and Astrophysics*, 436, 719
- Jones, H. R. A., Longmore, A. J., Allard, F., & Hauschildt, P. H. 1996, *MNRAS*, 280, 77
- Kirkpatrick, J. D. 2005, *ARA&A*, 43, 195

- Kirkpatrick, J. D. et al. 1999, *Astrophysical Journal*, 519, 802
- Lisse, C. M., Chen, C. H., Wyatt, M. C., Morlok, A., Song, I., Bryden, G., & Sheehan, P. 2009, *ApJ*, 701, 2019
- Lodders, K. 1999, *Astrophysical Journal*, 519, 793
- . 2002, *Astrophysical Journal*, 577, 974
- . 2003, *Astrophysical Journal*, 591, 1220
- . 2004, *Science*, 303, 323
- . 2009, arXiv: 0910.0811
- Lodders, K., & Fegley, Jr., B. 2002, *Icarus*, 155, 393
- . 2006, *Chemistry of Low Mass Substellar Objects*, ed. J. W. Mason (Springer Verlag)
- Marley, M. S., Saumon, D., Guillot, T., Freedman, R. S., Hubbard, W. B., Burrows, A., & Lunine, J. I. 1996, *Science*, 272, 1919
- McLean, I. S., McGovern, M. R., Burgasser, A. J., Kirkpatrick, J. D., Prato, L., & Kim, S. S. 2003, *Astrophysical Journal*, 596, 561
- Meléndez, J., & Barbuy, B. 1999, *Astrophysical Journals*, 124, 527
- Nakajima, T., Tsuji, T., & Yanagisawa, K. 2004, *Astrophysical Journal*, 607, 499
- Reid, I. N., Kirkpatrick, J. D., Gizis, J. E., Dahn, C. C., Monet, D. G., Williams, R. J., Liebert, J., & Burgasser, A. J. 2000, *Astronomical Journal*, 119, 369
- Robie, R. A., & Hemingway, B. S. 1995, *Thermodynamic Properties of Minerals and Related Substances at 298.15 K and 1 Bar (10^5 Pascals) Pressure and at Higher Temperatures (USGS Bulletin 2131)*
- Tsuji, T., Ohnaka, K., & Aoki, W. 1996, *Astronomy and Astrophysics*, 305, L1
- Visscher, C., Lodders, K., & Fegley, Jr., B. 2006, *Astrophysical Journal*, 648, 1181
- Weck, P. F., Schweitzer, A., Stancil, P. C., Hauschildt, P. H., & Kirby, K. 2003, *Astrophysical Journal*, 582, 1059

Table 1. Iron Gas Abundances

gas M	$\log X_M \approx$	reaction no.
Below iron cloud		
Fe	$-4.24 + [\text{Fe}/\text{H}]$	\dots
FeH	$-6.13 - 1905/T + 0.5 \log P_T + [\text{Fe}/\text{H}]$	7
FeOH	$-9.80 + 2468/T + 0.5 \log P_T + 2[\text{Fe}/\text{H}]$	11
Fe(OH) ₂	$-16.64 + 12088/T + \log P_T + 3[\text{Fe}/\text{H}]$	4
FeO	$-7.20 - 4713/T + 2[\text{Fe}/\text{H}]$	15
FeS	$-8.52 + 964/T + 2[\text{Fe}/\text{H}]$	16
Above iron cloud		
Fe	$7.23 - 20995/T - \log P_T$	1
FeH	$5.34 - 22900/T - 0.5 \log P_T$	7
FeOH	$5.02 - 18527/T - 0.5 \log P_T + 2[\text{Fe}/\text{H}] + \log X'_{\text{H}_2\text{O}}$	11
Fe(OH) ₂	$1.53 - 8907/T + 2[\text{Fe}/\text{H}] + 2 \log X'_{\text{H}_2\text{O}}$	3
FeO	$7.62 - 25708/T - \log P_T + [\text{Fe}/\text{H}] + \log X'_{\text{H}_2\text{O}}$	15
FeS	$2.96 - 20031/T - \log P_T + [\text{Fe}/\text{H}]$	16

Note. — $X'_{\text{H}_2\text{O}}$ is defined as the H_2O mole fraction in a solar-metallicity gas, where $\log X'_{\text{H}_2\text{O}} \approx -3.12$ within the CH_4 field and ≈ -3.58 within the CO field. The effect of metallicity on the atmospheric water abundance ($X_{\text{H}_2\text{O}}$) is included in the abundance equations. Expressions are valid for temperatures between 800 and 2500 K and metallicities up to $[\text{Fe}/\text{H}] = +0.5$ dex.

Table 2. Magnesium Gas Abundances

gas M	$\log X_M \approx$	reaction no.
Below magnesium-silicate clouds		
Mg	$-4.15 + [\text{Fe}/\text{H}]$...
MgH	$-5.46 - 4236/T + 0.5 \log P_T + [\text{Fe}/\text{H}]$	27
MgOH	$-8.98 + 1672/T + 0.5 \log P_T + 2[\text{Fe}/\text{H}]$	28
Mg(OH) ₂	$-15.54 + 10267/T + \log P_T + 3[\text{Fe}/\text{H}]$	22
MgO	$-6.12 - 7306/T + 2[\text{Fe}/\text{H}]$	29
MgS	$-7.94 + 2[\text{Fe}/\text{H}]$	30
Above magnesium-silicate clouds		
Mg	$8.25 - 27250/T - \log P_T - [\text{Fe}/\text{H}] - \log X'_{\text{H}_2\text{O}}$	17, 19
MgH	$6.94 - 31486/T - 0.5 \log P_T - [\text{Fe}/\text{H}] - \log X'_{\text{H}_2\text{O}}$	27
MgOH	$6.75 - 25578/T - 0.5 \log P_T$	28
Mg(OH) ₂	$3.53 - 16983/T + [\text{Fe}/\text{H}] + \log X'_{\text{H}_2\text{O}}$	22
MgO	$9.63 - 34556/T - \log P_T$	29
MgS	$4.40 - 27250/T - \log P_T - \log X'_{\text{H}_2\text{O}}$	30

Note. — $X'_{\text{H}_2\text{O}}$ is defined as the H₂O mole fraction in a solar-metallicity gas, where $\log X'_{\text{H}_2\text{O}} \approx -3.12$ within the CH₄ field and ≈ -3.58 within the CO field. The effect of metallicity on the atmospheric water abundance ($X_{\text{H}_2\text{O}}$) is included in the abundance equations. Expressions are valid for temperatures between 800 and 2500 K and metallicities up to $[\text{Fe}/\text{H}] = +0.5$ dex.

Table 3. Silicon Gas Abundances

gas M	$\log X_M \approx$	reaction no.
Below magnesium-silicate clouds; within SiO field		
SiO	$-4.20 + [\text{Fe}/\text{H}]$...
SiS	$-5.59 + 666/T + 2[\text{Fe}/\text{H}]$	44
Si	$-0.44 - 44738/T$	45
SiH	$-2.64 - 11500/T + 0.5 \log P_T$	46
SiH ₂	$-5.83 - 6422/T + \log P_T$	47
SiH ₃	$-8.97 - 2770/T + 1.5 \log P_T$	48
SiH ₄	$-13.33 + 6172/T + 2 \log P_T$	31
SiH ₃ F	$-20.57 + 13120/T + 2 \log P_T + [\text{Fe}/\text{H}]$	35
SiH ₂ F ₂	$-28.25 + 20160/T + 2 \log P_T + 2[\text{Fe}/\text{H}]$	39
Above magnesium-silicate clouds		
SiO	$10.09 - 28817/T - \log P_T - [\text{Fe}/\text{H}] - \log X'_{\text{H}_2\text{O}}$	17, 19
SiS	$5.38 - 28151/T - \log P_T - [\text{Fe}/\text{H}] - 2 \log X'_{\text{H}_2\text{O}}$	44
Si	$10.45 - 44659/T - \log P_T - 2[\text{Fe}/\text{H}] - 2 \log X'_{\text{H}_2\text{O}}$	45
SiH	$8.30 - 40317/T - 0.5 \log P_T - 2[\text{Fe}/\text{H}] - 2 \log X'_{\text{H}_2\text{O}}$	46
SiH ₂	$5.11 - 35239/T - 2[\text{Fe}/\text{H}] - 2 \log X'_{\text{H}_2\text{O}}$	47
SiH ₃	$1.97 - 31587/T + 0.5 \log P_T - 2[\text{Fe}/\text{H}] - 2 \log X'_{\text{H}_2\text{O}}$	48
SiH ₄	$-2.39 - 22645/T + \log P_T - 2[\text{Fe}/\text{H}] - 2 \log X'_{\text{H}_2\text{O}}$	31
SiH ₃ F	$-9.63 - 15697/T + \log P_T - [\text{Fe}/\text{H}] - 2 \log X'_{\text{H}_2\text{O}}$	35
SiH ₂ F ₂	$-17.31 - 8657/T + \log P_T - 2 \log X'_{\text{H}_2\text{O}}$	39

Note. — $X'_{\text{H}_2\text{O}}$ is defined as the H₂O mole fraction in a solar-metallicity gas, where $\log X'_{\text{H}_2\text{O}} \approx -3.12$ within the CH₄ field and ≈ -3.58 within the CO field. The effect of metallicity on the atmospheric water abundance ($X_{\text{H}_2\text{O}}$) is included in the abundance equations. Expressions are valid for temperatures between 800 and 2500 K and metallicities up to $[\text{Fe}/\text{H}] = +0.5$ dex.

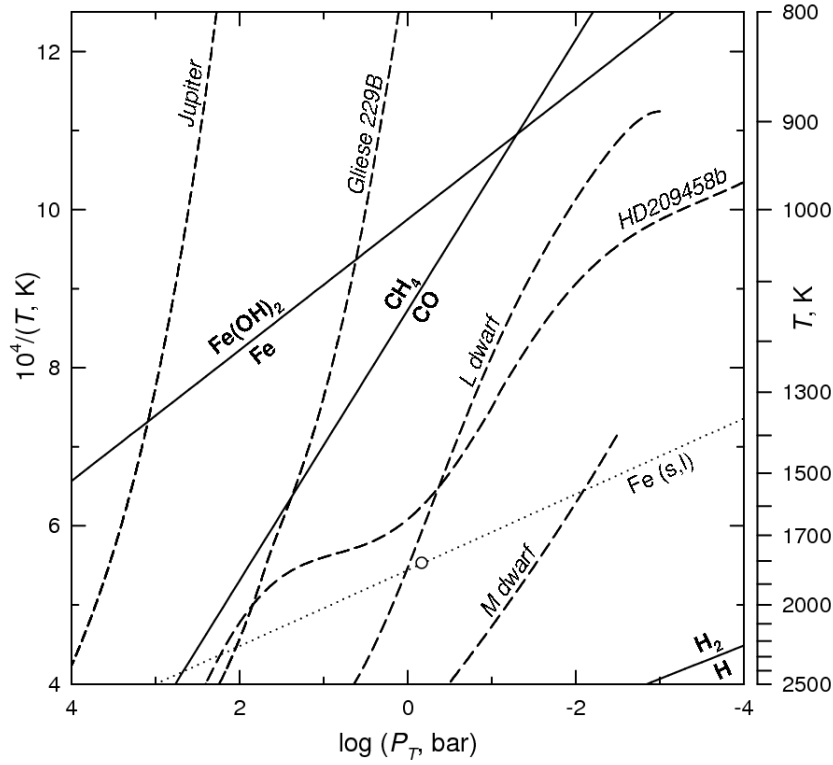


Fig. 1.— Overview of iron chemistry as a function of temperature and pressure in a protosolar composition gas. The solid line indicates where Fe and $\text{Fe}(\text{OH})_2$ have equal abundances. The dotted line labeled Fe(s,l) is the condensation curve for iron, with an open circle denoting its normal melting point (1809 K). Also shown are model atmospheric profiles for representative substellar objects (dashed lines). See text for details.

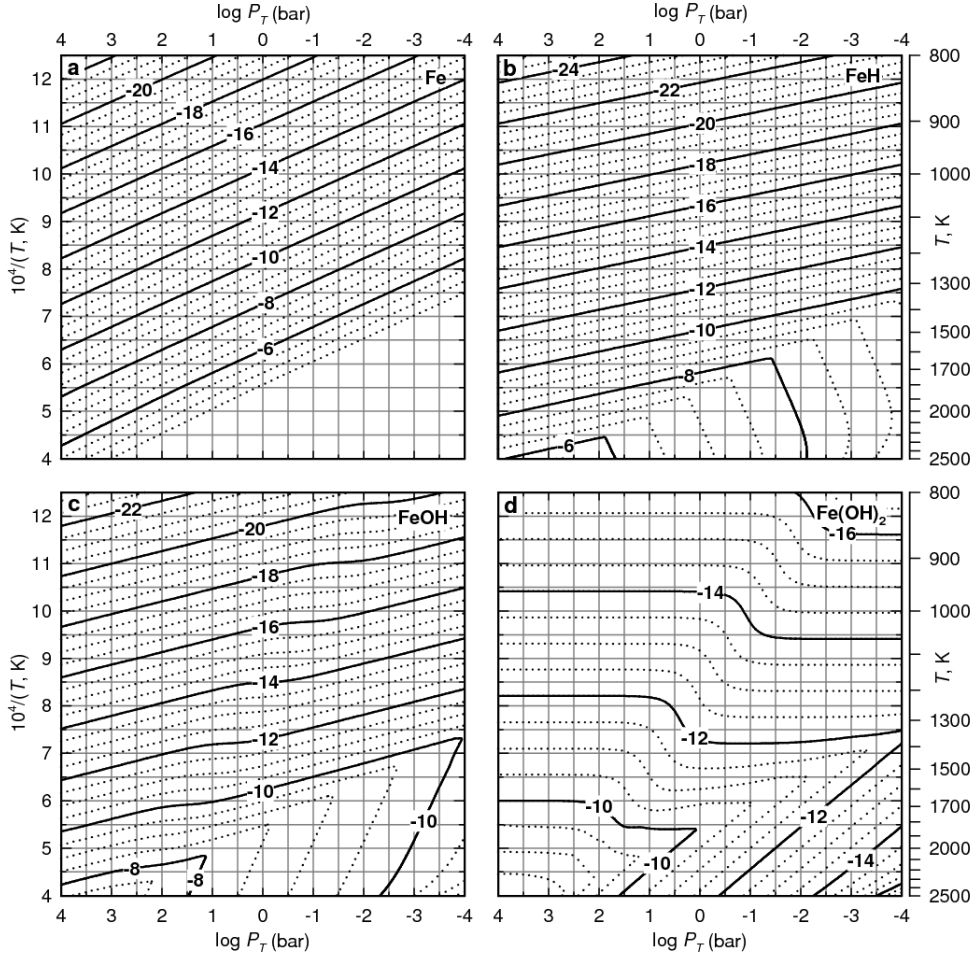


Fig. 2.— Mole fraction contours (on a logarithmic scale) for (a) monatomic iron (Fe), (b) iron hydride (FeH), (c) iron monohydroxide (FeOH), and (d) iron hydroxide (Fe(OH)₂) as a function of pressure and temperature in a solar-metallicity gas. The kinks in the abundance contours are due to Fe metal or liquid condensation.

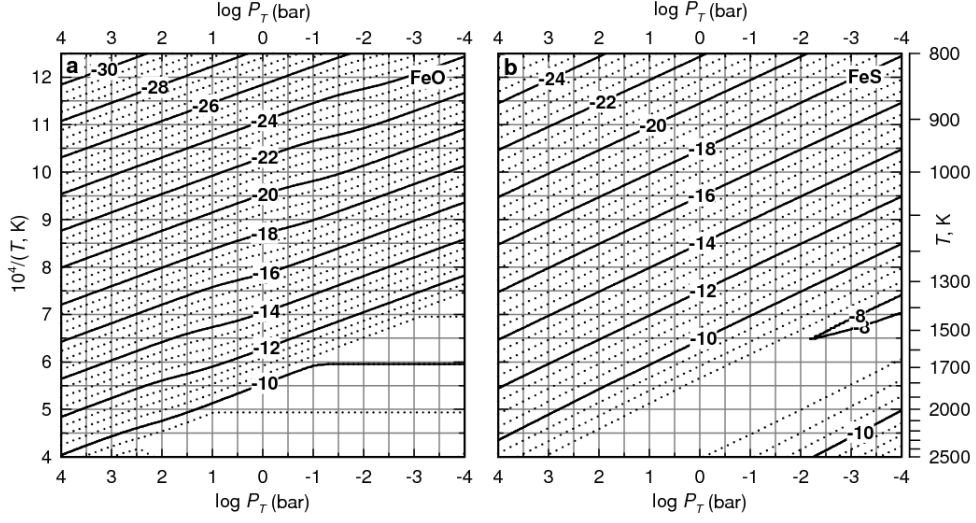


Fig. 3.— Mole fraction contours (on a logarithmic scale) for (a) iron monoxide (FeO) and (b) iron sulfide (FeS) as a function of pressure and temperature in a solar-metallicity gas.

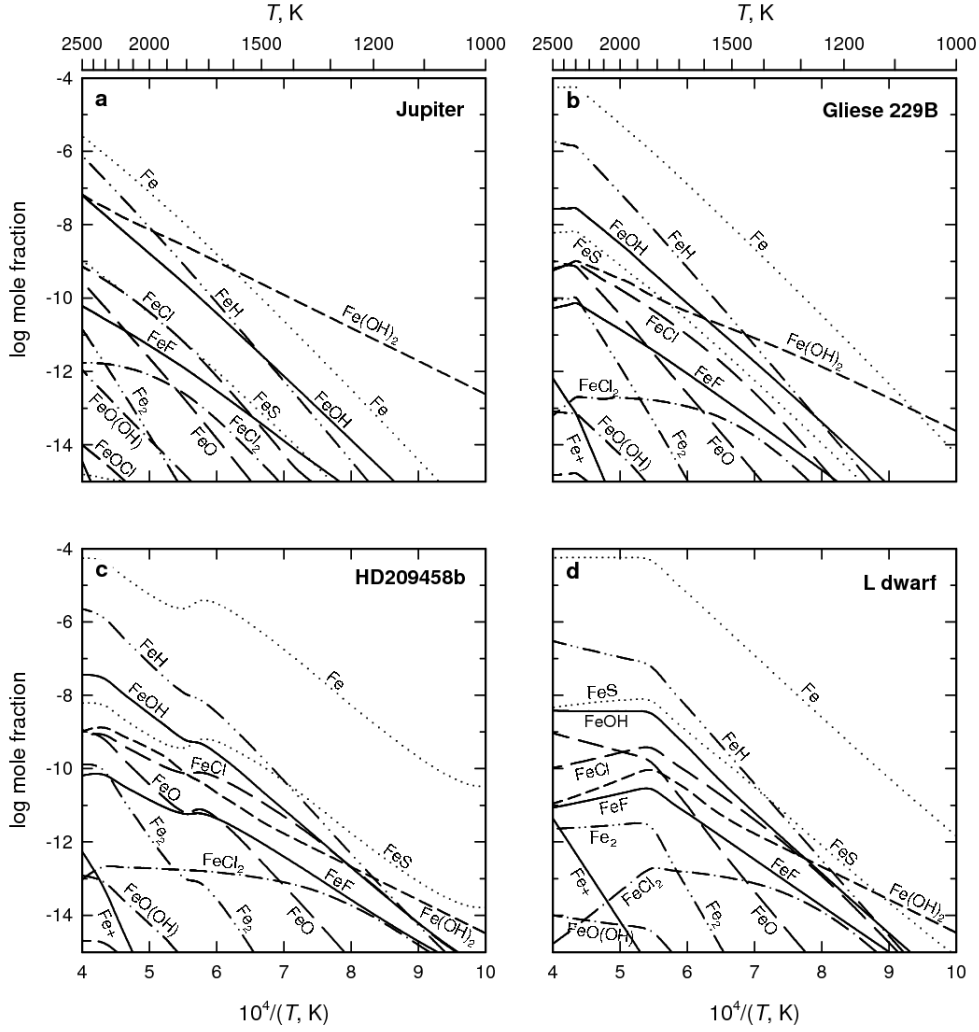


Fig. 4.— Iron chemistry along the atmospheric pressure-temperature profile from 1000 to 2500 K for (a) Jupiter, (b) Gliese 229B, (c) HD209458b, and (d) an L dwarf ($T_{\text{eff}} = 1800$ K). Breaks in the Fe curves show where Fe condenses (b,d). Iron is condensed throughout the entire temperature range shown here for Jupiter and HD209458b (a,c).

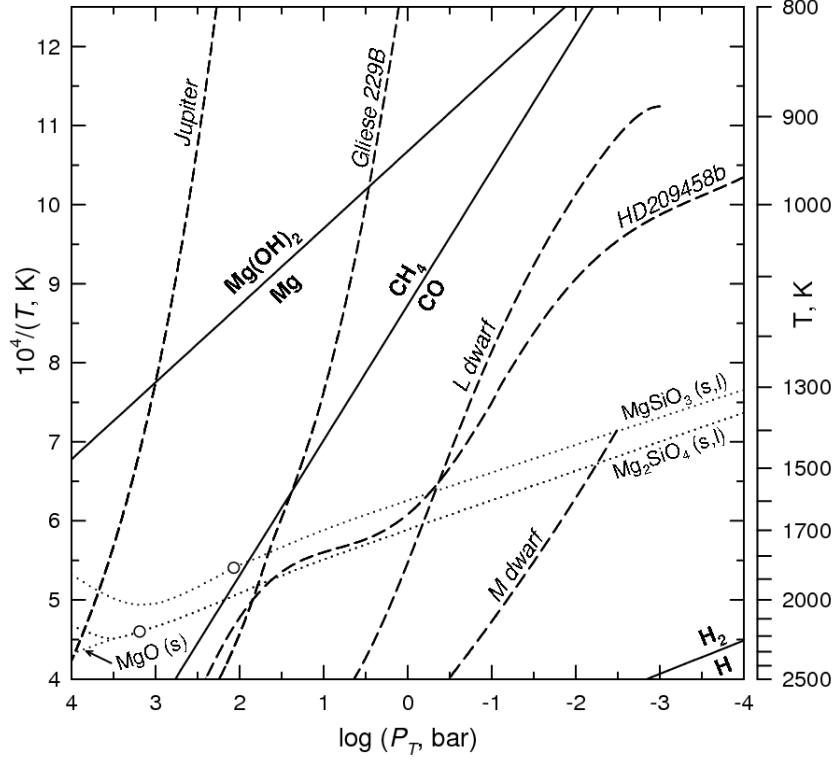


Fig. 5.— Overview of magnesium chemistry as a function of temperature and pressure in a protosolar composition gas. The solid line indicates where Mg and Mg(OH)_2 have equal abundances. The dotted lines labeled $\text{Mg}_2\text{SiO}_4(\text{s,l})$ and $\text{MgSiO}_3(\text{s,l})$ show the condensation temperatures of forsterite and enstatite, with circles denoting their normal melting points of 1803 K (enstatite) and 2163 K (forsterite). The dotted line labeled MgO(s) is the condensation curve for periclase. See text for details.

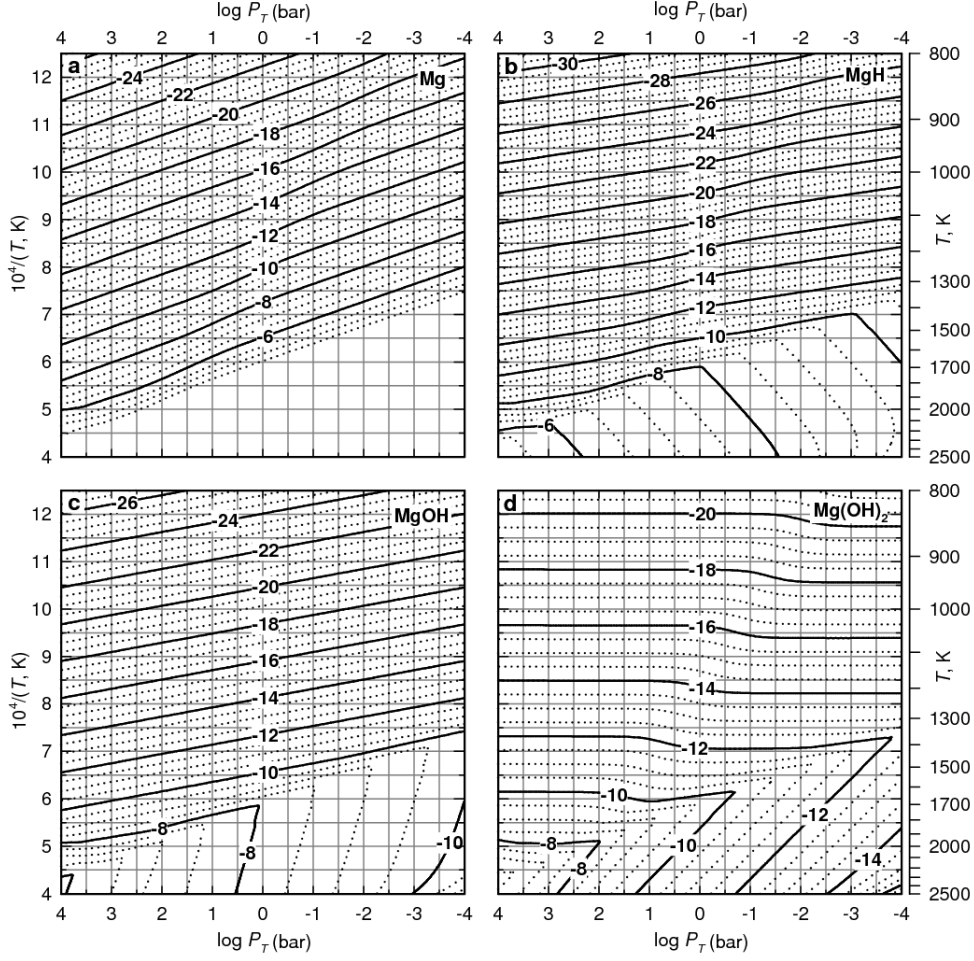


Fig. 6.— Mole fraction contours (on a logarithmic scale) for (a) monatomic magnesium (Mg), (b) magnesium hydride (MgH), (c) magnesium monohydroxide (MgOH), and (d) magnesium hydroxide ($\text{Mg}(\text{OH})_2$) as a function of pressure and temperature in a solar-metallicity gas. The kinks in the abundance contours occur at the condensation temperature of Mg_2SiO_4 (forsterite).

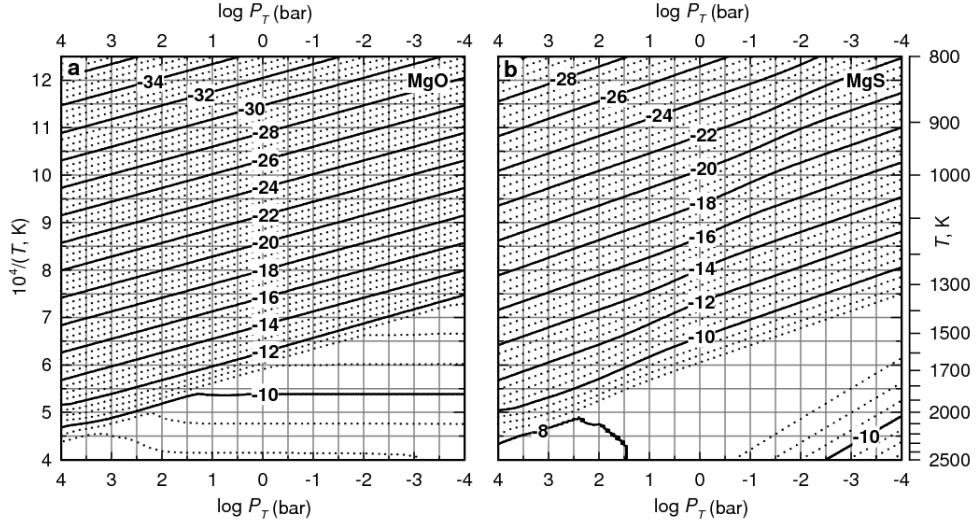


Fig. 7.— Mole fraction contours (on a logarithmic scale) for (a) magnesium monoxide (MgO) and (b) magnesium sulfide (MgS) as a function of pressure and temperature in a solar-metallicity gas.

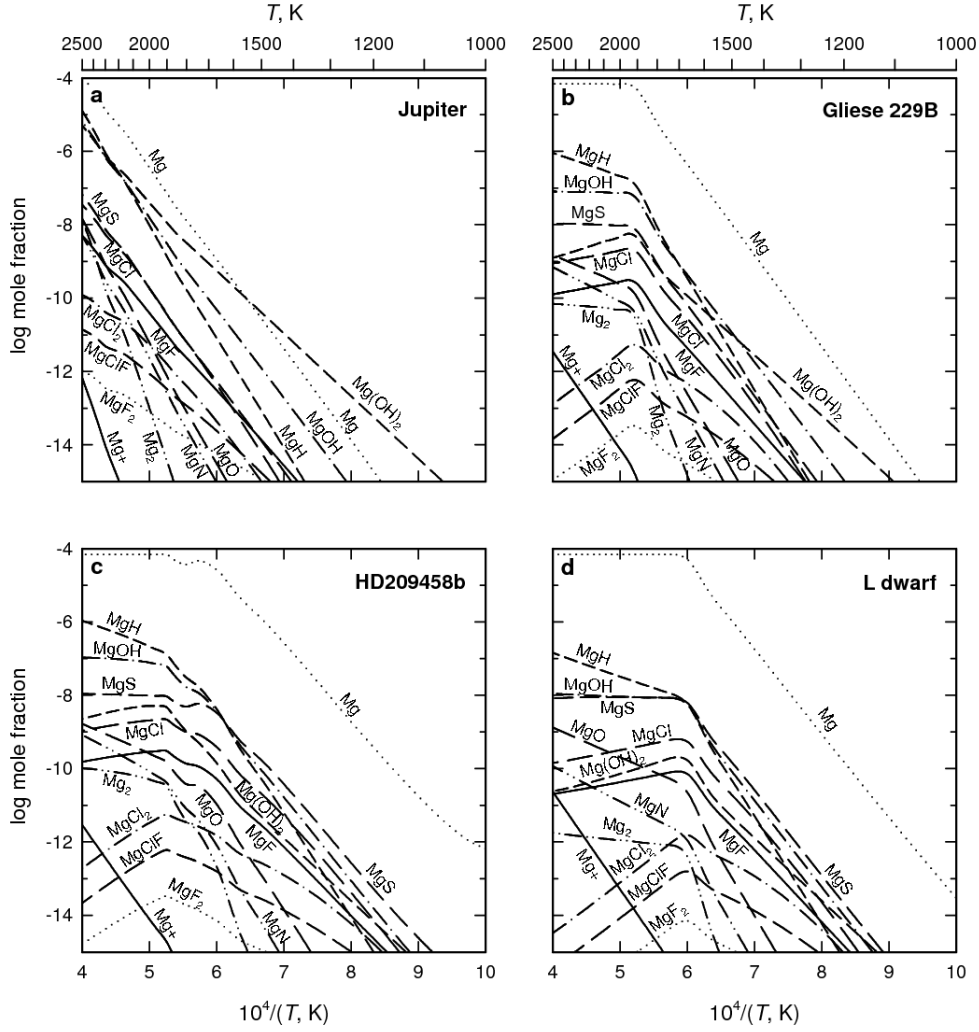


Fig. 8.— Magnesium chemistry along the atmospheric pressure-temperature profile from 1000 to 2500 K for (a) Jupiter, (b) Gliese 229B, (c) HD209458b, and (d) an L dwarf ($T_{\text{eff}} = 1800$ K). Breaks in the Mg curves show where magnesium-silicates condense (b,c,d). Forsterite is condensed throughout the entire temperature range shown here for Jupiter (a).

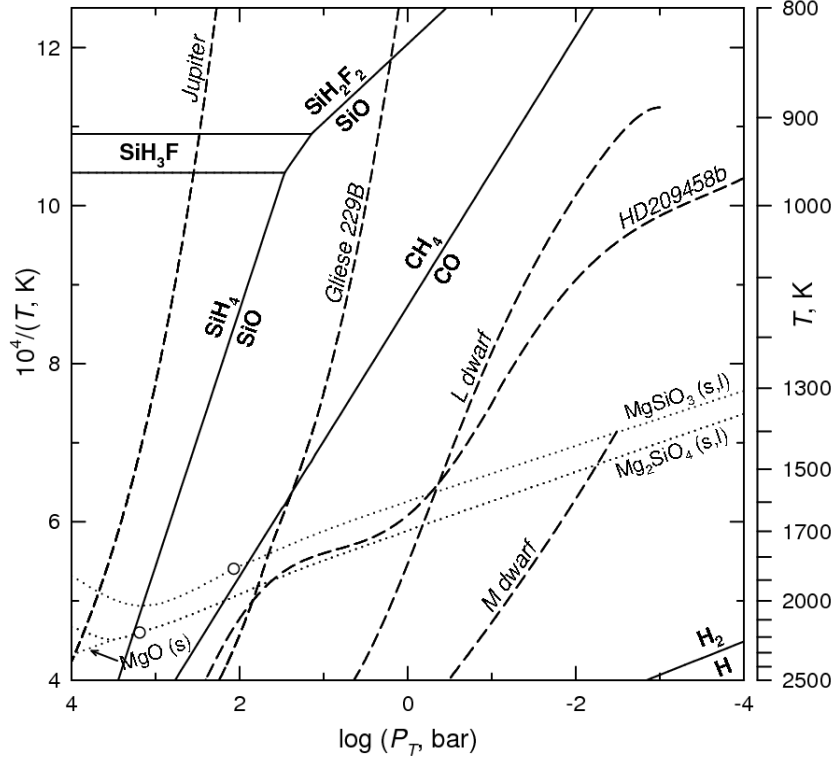


Fig. 9.— Overview of silicon chemistry as a function of temperature and pressure in a protosolar composition gas. The solid line indicates where dominant Si-bearing gases have equal abundances. The dotted lines labeled Mg_2SiO_4 and MgSiO_3 show the condensation temperatures of forsterite and enstatite, with circles denoting their melting points. Also shown are model atmospheric profiles for representative substellar objects (dashed lines). See text for details.

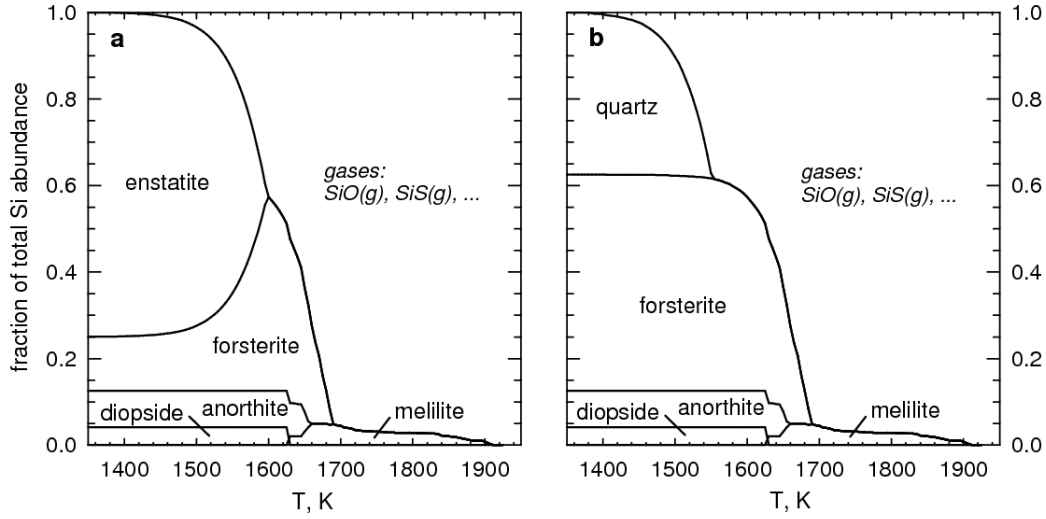


Fig. 10.— Elemental distribution of silicon into condensed phases at 1 bar in a solar-metallicity gas with enstatite (MgSiO₃) formation a) included or b) suppressed. Quartz (SiO₂) condensation will only proceed in the absence of enstatite, which otherwise efficiently removes silicon from the gas phase. The silicates melilite, anorthite, and diopside together consume up to $\sim 12\%$ of the total Si abundance. SiO and SiS are the dominant Si-bearing gases before removal by condensation.

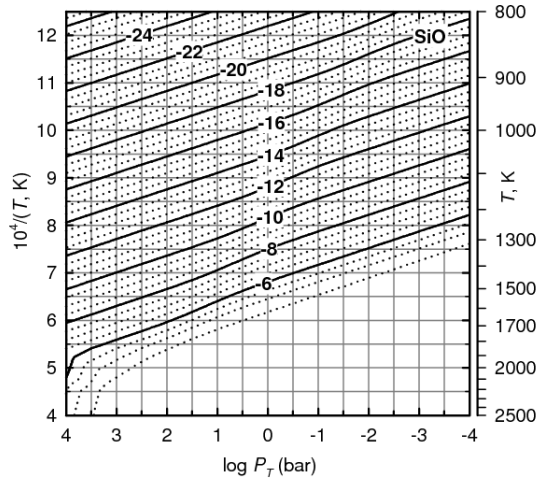


Fig. 11.— Mole fraction contours (on a logarithmic scale) for silicon monoxide (SiO) as a function of pressure and temperature in a solar-metallicity gas.

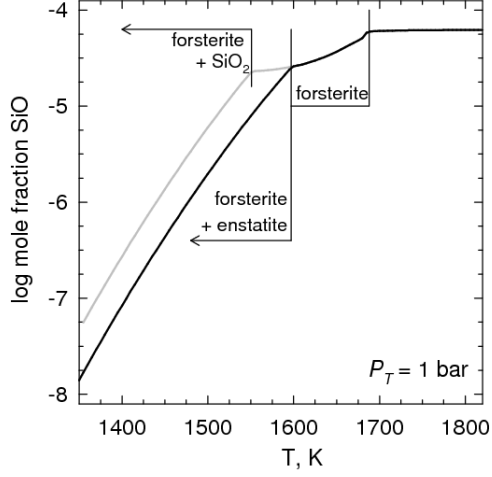


Fig. 12.— Mole fraction abundance of SiO gas at 1 bar total pressure in a solar-metallicity gas with enstatite formation included (black line) or suppressed (gray line) above the forsterite cloud layer. The formation of SiO_2 instead of MgSiO_3 would yield larger mole fraction abundances of SiO gas above the clouds.

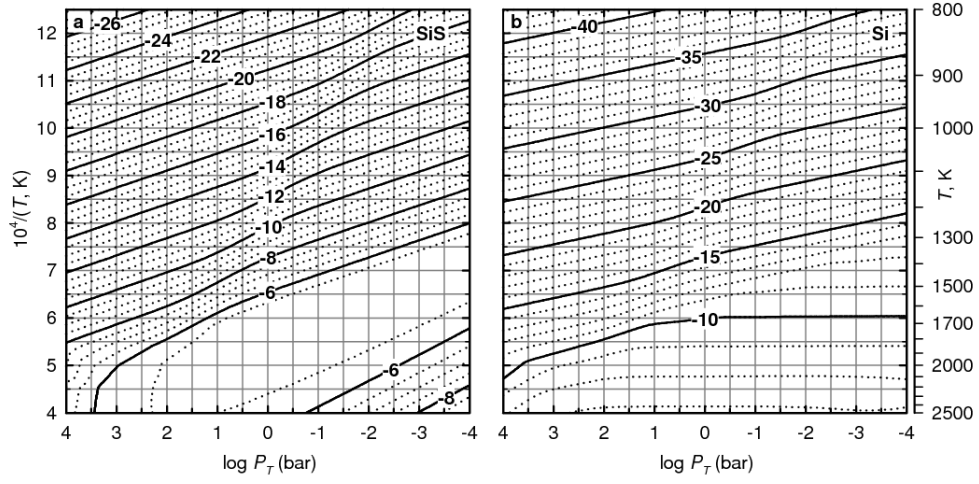


Fig. 13.— Mole fraction contours (on a logarithmic scale) for (a) silicon monosulfide (SiS) and (b) monatomic silicon (Si) as a function of pressure and temperature in a solar-metallicity gas.

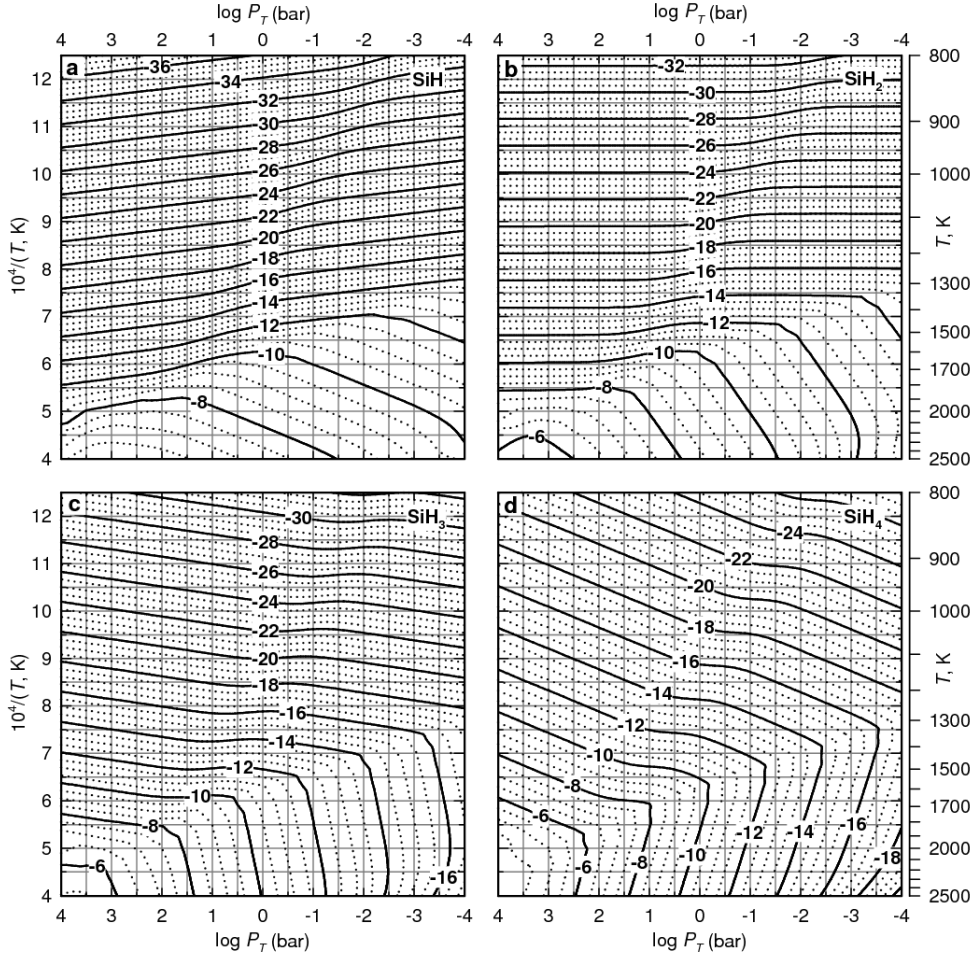


Fig. 14.— Mole fraction contours (on a logarithmic scale) for (a) silyldiyne (SiH), (b) silylene (SiH₂), (c) the silyl radical (SiH₃), and (d) silane (SiH₄) as a function of pressure and temperature in a solar-metallicity gas. The bends in the abundance contours occur where magnesium silicate clouds (MgSiO₃, Mg₂SiO₄) condense.

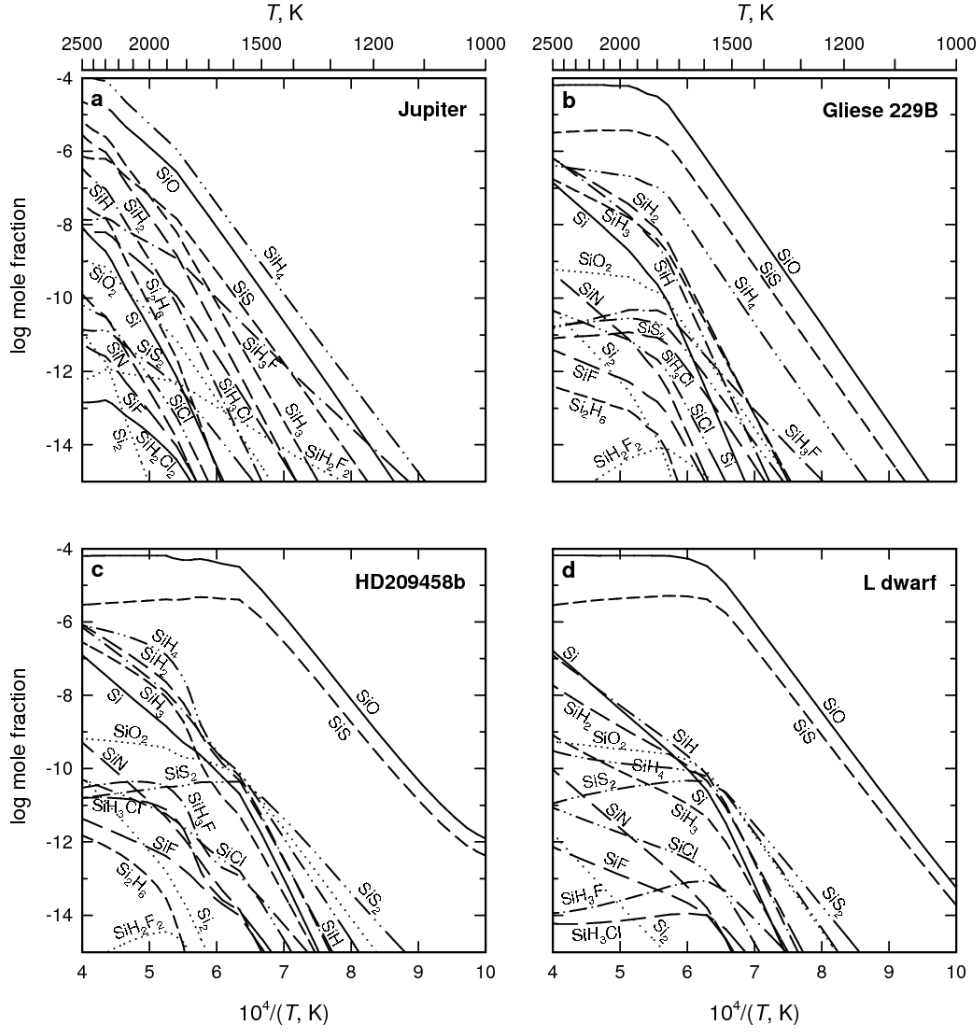


Fig. 15.— Silicon chemistry along the atmospheric pressure-temperature profile from 1000 to 2500 K for (a) Jupiter, (b) Gliese 229B, (c) HD209458b, and (d) an L dwarf ($T_{\text{eff}} = 1800$ K). Breaks in the SiO curves show where magnesium-silicates condense (b,c,d). Forsterite is condensed throughout the entire temperature shown here for Jupiter (a).